Acta Pharmaceutica Sinica B 2025;15(5):2687−2702

Chinese Pharmaceutical Association
Institute of Materia Medica, Chinese Academy of Medical Sciences

Acta Pharmaceutica Sinica B

www.elsevier.com/locate/apsb
www.sciencedirect.com

ORIGINAL ARTICLE

Celastrol-loaded ginsenoside Rg3 liposomes boost immunotherapy by remodeling obesity-related immunosuppressive tumor microenvironment in melanoma

Hongyan Zhang[a,b,†], Jingyi Huang[a,†], Yujie Li[a,†], Wanyu Jin[a], Jiale Wei[a], Ninghui Ma[a], Limei Shen[c], Mancang Gu[a,b], Chaofeng Mu[a], Donghang Xu[d,*], Yang Xiong[a,b,*]

[a]*School of Pharmaceutical Sciences, Zhejiang Chinese Medical University, Hangzhou 310053, China*
[b]*Academy of Chinese Medical Science, Zhejiang Chinese Medical University, Hangzhou 310053, China*
[c]*Division of Molecular Pharmaceutics, Eshelman School of Pharmacy, University of North Carolina at Chapel Hill, Chapel Hill, NC 27599, USA*
[d]*Department of Pharmacy, the Second Affiliated Hospital, Zhejiang University School of Medicine, Hangzhou 310053, China*

Received 18 October 2024; received in revised form 10 January 2025; accepted 2 February 2025

KEY WORDS

Obesity related tumor;
Immunosuppressive tumor microenvironment;
Celastrol;
Rg3-liposome;
Glucose transporter 1;
Immunogenic cell death;
Metabolic reprogramming;
Immunotherapy

Abstract Obesity usually exacerbates the immunosuppressive tumor microenvironment (ITME), hindering $CD8^+$ T cell infiltration and function, which further represents a significant barrier to the efficacy of immunotherapy. Herein, a multifunctional liposomal system (CR-Lip) for encapsulating celastrol (CEL) was utilized to remodel obesity-related ITME and improve cancer immunotherapy, wherein Ginsenoside Rg3 (Rg3) was detected interspersed in the phospholipid bilayer and its glycosyl exposed on the surface of the liposome. CR-Lip had a relatively uniform size (116.5 nm), facilitating favorable tumor tissue accumulation through the interaction between Rg3 and glucose transporter 1 overexpressed in obese tumor cells. Upon reaching the tumor region, CR-Lip was found to induce the immunogenic cell death (ICD) of HFD tumor cells. Notably, the level of PHD3 in HFD tumor cells was effectively boosted by CR-Lip to effectively block metabolic reprogramming and increase the availability of major free fatty acids fuel sources. *In vivo*, experiments studies revealed that the easy-obtained nano platform stimulated enhanced the production of various cytokines in tumor tissues, DC maturation, $CD8^+$ T-cell infiltration,

*Corresponding authors.
E-mail addresses: xudonghang@zju.edu.cn (Donghang Xu), xiongyang@zcmu.edu.net (Yang Xiong).
†These authors made equal contributions to this work.

Peer review under the responsibility of Chinese Pharmaceutical Association and Institute of Materia Medica, Chinese Academy of Medical Sciences.

https://doi.org/10.1016/j.apsb.2025.03.017

and synergistic anticancer therapeutic potency with aPD-1 (tumor inhibition rate = 82.1%) towards obesity-related melanoma. Consequently, this study presented an efficacious approach to tumor immunotherapy in obese mice by encompassing tumor eradication, inducing ICD, and reprogramming metabolism. Furthermore, it offered a unique insight into a valuable attempt at the immunotherapy of obesity-associated related tumors.

1. Introduction

The prevalence of obesity has tripled since 1975, presenting a significant global health burden[1,2]. Evidence from numerous epidemiological studies shows that obesity is a driving force in many diseases and is causally related to an elevated risk of more than thirteen types of cancer[3−5]. Elevated levels of hormones, adipokines, and metabolic dysregulation are the principal causes of obesity-related cancers[4]. Notably, dietary perturbations altering nutrient availability and systemic metabolic state can also impact anti-tumor immunity responses[6,7]. Cancer immunotherapy has gained significant traction as a means to enhance systemic anti-tumor immune responses. However, 40−45% of clinical melanomas respond poorly to anti-PD-1/PD-L1(aPD-1/aPD-L1) therapy[8−10]. Obese patients, who make up a significant proportion, often show reduced immunotherapeutic efficacy due to the immunosuppressive tumor microenvironment (ITME) and impaired $CD8^+$ T cell function in cancers such as melanoma and breast cancer[7,11−13]. Therefore, addressing the ITME and restoring intratumoral $CD8^+$ T cells is crucial for treating obesity-associated cancers.

One effective strategy is to induce immunogenic cell death (ICD). During ICD, dying tumor cells release immunostimulatory danger signals[14] such as high mobility group box 1 (HMGB1)[15], calreticulin (CRT)[16], and adenosine triphosphate (ATP)[17], which stimulate dendritic cells (DCs) maturation. Subsequently, these DCs migrate to lymph nodes, where they engage in antigen presentation with naive $CD8^+$ T cells, initiating a specific T cell response[18,19]. However, in obese individuals, immune cell functions may be compromised. Chronic inflammation and metabolic changes caused by obesity can lead to phenotypic alterations and functional dysregulation of immune cells, potentially weakening their response to ICD and anti-tumor immunity[20,21]. Recent findings on tumor metabolism reveal that lipid metabolism plays a crucial role in immune evasion[7,22]. Specifically, tumor cells, but not $CD8^+$ T cells, respond to a high-fat diet (HFD) by downregulating prolyl hydroxylase-3 (PHD3), which hijacks free fatty acids (FFAs). PHD3, a member of the prolyl hydroxylase family, regulates hypoxia response, fatty acid oxidation, and the import of long-chain fatty acids into mitochondria[23,24]. This shift leads to an altered distribution of fuel between the populations of cells, affecting $CD8^+$ T cell activation and suppressing anti-tumor immunity during obesity. Therefore, exploring strategies to increase PHD3 expression in tumors is vital for improving ICD response and enhancing PD-1/PD-L1 immunotherapy efficacy in the obesity-related ITME.

Celastrol (CEL), a key active ingredient obtained from Tripterygium wilfordii, has demonstrated superior anti-cancer ability and potential as an ICD inducer, activating DCs and $CD8^+$ T cells[25−27]. Additionally, CEL has emerged as a promising drug for obesity treatment[28−30], regulating lipid metabolism in cancer through various mechanisms, including inhibiting lipid synthesis, promoting lipid catabolism, preventing lipid accumulation, regulating cholesterol metabolism, and influencing relevant signaling pathways[31,32]. This suggests that CEL could be an effective ICD inducer and lipid metabolism regulator for treating obesity-related cancer, enhancing $CD8^+$ T cell infiltration and function. However, CEL faces limitations in biosecurity, tumor targeting, and solubility.

To address these issues, we developed a CEL-loaded ginsenoside Rg3 (Rg3) liposome (CR-Lip) designed to precisely target tumor cells in the obesity-related ITME while maintaining robust immunological activity. This system aims to induce ICD and reprogram lipid metabolism in tumor cells, enhancing immune responses to anti-PD-1 therapy in obesity-related melanoma. We confirmed that glucose transporter 1 (GLUT1) is overexpressed in tumor cells, especially after obesity intervention. Extensive studies have shown that Rg3, containing two glycosyl residues, binds effectively to GLUT1 and serves as a suitable cholesterol substitute for liposome preparation[33−35]. Leveraging Rg3's tumor−selective properties, we established a functional Rg3-Lip loaded with CEL. *In vitro*, CR-Lip not only induced strong ICD in tumor cells but also reduced lipid levels, likely due to PHD3 upregulation. In B16−F10 tumor-bearing HFD mice, CR-Lip maintained CEL concentration in melanoma, alleviated the HFD-induced ITME, improved $CD8^+$ T cell infiltration and activation, downregulated immunosuppressive cells, and reduced adipocyte infiltration, significantly enhancing the response to anti-PD-1 therapy. Overall, this approach effectively inhibited tumor growth in obesity-related melanoma, sensitized immunotherapy, and extended mice survival, offering promising therapeutic options for overcoming obesity-related cancers.

2. Materials and methods

2.1. Materials

CEL was obtained from Bidepharm (Shanghai, China). Rg3 was obtained from Chengdu Master Biotechnology Co., Ltd. (Chengdu, China). Cholesterol (Cho) and soybean phospholipid (SPC) were provided by Advanced Vehicle Technology (Shanghai, China). Oil Red O Stain Kit was obtained from Solarbio (Beijing, China). Annexin V-FITC/PI Apoptosis Kit was gained from Vazyme (Nanjing, China). Coumarin 6 (C6) and DiR were purchased from Macklin (Shanghai, China). DiD, BODIPY 493/503, ATP, and TUNEL kits were obtained from Beyotime (Shanghai, China). Mouse 3T3-L1 cell adipogenic differentiation kit was purchased from OriCell (Guangzhou, China). The reverse Transcription Premix kit and SYBR Green qPCR kit were provided by Hangzhou Aikerui Biotechnology Co., Ltd. (Changsha, China).

Antibodies: aPD-1 (clones RMP1-14) were purchased from BioXcell (West Lebanon, NH). Supporting Information Tables S1 and S2 list antibodies and primers for Western blotting (WB), quantitative reverse transcription PCR (RT-qPCR), flow cytometry (FCM), and immunofluorescence (IF) staining.

Cell lines and experimental animals: The murine melanoma cell line B16−F10 and the 3T3-L1 cell lines were obtained from the American Type Culture Collection (ATCC, Manassas, VA). The C57BL/6 mice (female, 4 weeks old) were obtained from the Animal Experimental Research Centre of Zhejiang Chinese Medical University, in accordance with ethical permit No. IACUC-20230327-12. All animal studies were conducted in compliance with NIH guidelines for laboratory research and were authorized by the Animal Care Committee of Zhejiang Chinese Medical University.

2.2. Preparation of CR-Lip

Four types of liposomes, including Chol liposomes loaded with CEL (CEL-Lip), Chol-based liposomes without CEL (Cho-Lip), Rg3 and CEL co-loaded liposomes (CR-Lip), and Rg3-based liposomes without CEL (Rg3-Lip) were prepared by thin-film hydration method. The formulations included Cho/SPC/CEL (3:10:1, *w*/*w*/*w*) for CEL-Lip, Cho/SPC/CEL (3:10:0, *w*/*w*/*w*) for Cho-Lip, Rg3/SPC/CEL (3:10:1, *w*/*w*/*w*) for CR-Lip and Rg3/SPC/CEL (3:10:0, *w*/*w*/*w*) for Rg3-Lip. The membrane material was dissolved in a solution of organic compounds, comprising chloroform and ethanol in a 1:1 volume ratio, to a final volume of 3 mL. Subsequently, the mixtures were subjected to reduced pressure rotary evaporation using a rotary evaporator (N-1100-D, Davi Instrument, Hangzhou, China) for 30 min in a water bath at 50 °C. This process was employed to remove the organic solvent and facilitate the formation of thin and uniform lipid membranes. The administration of nitrogen was conducted in a manner that was both gentle and appropriate, with the objective of safeguarding the lipid membranes. Subsequently, the mixtures were hydrated in 4 mL of PBS (pH 7.4) for 30 min at 50 °C. Finally, the suspension was subjected to ultrasonication using an ultrasonicator (JY92-IIN, Xinzhi Biotechnology Co., Ltd., Ningbo, China) until it became semi-transparent (power 300 W, operation 3 s, intermittent operation 2 s, 60 cycles). Furthermore, fluorescently labeled liposomes (C6/DiR/DID) were obtained by separately adding the appropriate amount of C6/DiR/DID to the lipid solutions prior to evaporation.

2.3. Characterization, serum stability, and storage stability of CR-Lip

In order to ascertain the particle size and zeta potential of CEL-Lip and CR-Lip, the Zetasizer (Malvern, UK) was utilized. Meanwhile, the transmission electron microscope (TEM, H-7650, Hitachi, Japan) was employed to examine the morphology of the CEL-loaded liposome. The CEL encapsulation efficiency (EE%) and drug-loading capacity (DL%) were calculated as shown in Eqs. (1) and (2):

$$\mathrm{EE\%} = \frac{W_{\mathrm{en}}}{W_{\mathrm{t}}} \times 100 \tag{1}$$

$$\mathrm{DL\%} = \frac{W_{\mathrm{en}}}{W_{\mathrm{l}}} \times 100 \tag{2}$$

The variables were defined as follows: W_{en} was the actual amount of encapsulated CEL of CEL-loaded Lips; W_{t} was the gross drug added to CEL-loaded Lips; W_{l} is the aggregate mass of CEL-loaded Lips; The prepared CEL-loaded Lips were stored at 4 °C to examine storage stability by measuring size and PDI for a week. The serum stability of CR-Lip was assessed through incubation with 10% FBS at 37 °C, with changes in particle size and PDI recorded over a 24 h period.

2.4. In vitro release of CEL from CR-Lip

The release of CEL from CEL-loaded Lips (CEL-Lip and CR-Lip) in pH 7.4 media (containing 0.2% *w*/*v* Tween 80) was examined by dialysis. In brief, 1.0 mL (100 mg/mL) of CEL-loaded Lips solutions ($n = 3$) were placed into the dialysis bag (MWCO = 3500). The dialysis pouch was then immersed in 20 mL of release medium at the desired pH, which should be agitated at 37 °C and 100 rpm. At designated time points, 2 mL of the release medium was sampled and replaced with an equal volume of fresh blank medium, the CEL concentration can be assessed by High-performance liquid chromatography (HPLC, Agilent, USA)[26].

2.5. Preparation of mature adipocytes and collection of mature adipocytes-conditioned medium (Adip-CM)

For adipocyte differentiation, mature adipocytes were induced to differentiate by adipogenic differentiation kit. In brief, 3T3-L1 cells were cultivated for a further two days after confluence (designated as Day 0), and differentiation A was added for 3 days. Then, the medium was changed with maintenance B for 1 day. Next, A and B should be used alternately 3 times, and the cell status should be observed daily during this period. Following the differentiation of 3T3-L1 cells, the acquisition of the adipocyte phenotype was confirmed through Oil Red O staining.

To collect conditioned medium (CM) from Adip-CM, maintenance B was replaced with fresh complete medium after 2 days, collected, and centrifuged at −20 °C[36−39]. In order to simulate the obesity-related TME *in vitro*, B16−F10 cells were pre-intervened with 50% Adip-CM for 24 h for subsequent trials.

2.6. Colony formation assay

In order to conduct the colony formation assay, B16−F10 cells were seeded at 400 cells per well into a 6-well plate and subsequently incubated for a period of 48 h. Subsequently, the cells are cultivated in complete or 50% Adip-CM for a further two days. Cells are maintained in complete or 50% Adip-CM for another 2 days. Then the B16−F10 cells were grown for another 10−12 days, with the culture medium being replaced on a tri-weekly basis. After 14 days, the cells were subjected to a fixation and staining procedure with 0.05% crystal violet. A colony comprising 50 or more cells was deemed to be a clone. The images were then digitally captured and the number of colonies formed was quantified using the ImageJ software.

2.7. Cellular uptake of CEL-loaded Lips in B16−F10 cells intervened by Adip-CM

For the glucose transporter inhibitor experiment, B16−F10 cells (2×10^5 cells/well) were seeded into 6-well plates. First, glucose (GLU, 20 μmol/L) or quercetin solution (20 mg/mL) was added to the cells for 60 min in advance. Subsequently, Rg3/C6-Lip and Cho/C6-Lip were added and incubated for 4 h. After incubation,

B16−F10 cells were collected and examined using FCM (CytoFlex S, Beckman, USA).

For cellular uptake, B16−F10 cells (2×10^5 cells/well) were intervened by Adip-CM for 24 h, then incubated with Cho/C6-Lip and Rg3/C6-Lip for 2 or 4 h. Then, B16−F10 cells were harvested and quantified by FCM. In addition, fluorescence microscopic observation (LSM 880, Zeiss, Germany) was taken for qualitative research.

2.8. *In vitro cytotoxicity and apoptosis*

B16−F10 cells (3000 cells/well, pre-intervened by Adip-CM for 24 h) were incubated with Free CEL, Free CEL + Rg3, CEL-Lip, and CR-Lip for 24 h at designed concentrations of CEL (0.1,0.2, 0.4, 0.8, 1.6, 3.2 and 6.4 μmol/L), respectively. HFD B16−F10 cells were incubated with methyl thiazolyl tetrazolium (MTT) for 4 h and solubilized with DMSO (150 μL). Absorbance was monitored at 570 nm by a multifunctional plate reader (EnSpire, PerkinElmer, USA). The Annexin V-FITC/PI Apoptosis Assay was employed for the assessment of the apoptotic level. In short, B16−F10 cells (2×10^5 cells/well, pre-intervened by Adip-CM) were incubated with free CEL, CEL-Lip, and CR-Lip for 12 h. These experiments employed 1 μmol/L CEL for B16−F10 cells. Cells were collected and suspended in a binding buffer. Then, Annexin V-FITC (5 μL) and PI solution (5 μL) were added and incubated. Subsequently, samples (500 μL) were examined by FCM without delay.

2.9. *BODIPY staining*

The lipid content of the cells was assessed using BODIPY 493/503. B16−F10 cells (1.5×10^4 cells/well) were incubated with free CEL at three concentrations (0.4, 0.8 and 1.2 μmol/L) for one day. Then cells were treated with Adip-CM for 24 h. For quantitative analysis, all groups were harvested and further incubated with BODIPY 493/503 (2.5 μmol/L) for 15 min at room temperature (RT). After that, the cells underwent two washes and were immediately analyzed by FCM. For confocal laser scanning microscopy (CLSM) analysis, B16−F10 cells (3×10^3/well) were seeded onto 24-well plates and cultured with CEL-Lip and CR-Lip (equivalent CEL concentration 0.8 μmol/L) for 24 h. After this, all groups were fixed and permeabilized with 0.2% TritonX-100 for 5 min. Next, B16−F10 cells were incubated with BODIPY 493/503 for 15 min. After washing with PBS and staining with DAPI, the cells were imaged using CLSM.

2.10. *The animal experiments*

2.10.1. *Mouse obesity models*

In all *in vivo* trials, C57/BL6 mice were maintained on a control diet (CD) or on a HFD for 8−10 weeks at the age of 5 weeks old. To measure plasma triglyceride (TG), Cho, and GLU concentrations after feeding CD or HFD, the mice were fasted overnight and whole blood was obtained by cardiac puncture into tubes containing EDTA (0.5 mol/L). Whole blood was centrifuged ($1500 \times g$, 20 min, 4 °C) and the plasma supernatant was transferred to new tubes for analysis.

2.10.2. *Tumor targeting efficacy of CR-Lip in B16−F10 tumor-bearing CD/HFD mouse model*

Prepare DIR@Cho-Lip or DIR@Rg3-Lip as described in 2.2. At the tumor volume (V_t) of approximately 80 mm^3, the CD or HFD mice bearing B16−F10 were injected with DIR@Cho-Lip or DIR@Rg3-Lip (100 μL) through the tail vein. *In vivo* fluorescence imaging was conducted using an imaging system (Caliper Life Sciences, USA) at 2, 4, 8, 12, and 24 h post-injection (Em = 745 nm; Ex = 810 nm). Tumors and major organs were then harvested for *ex vivo* fluorescence imaging. To visualize the co-localization of DIR@Rg3-Lip with GLUT1, tumor sections were first incubated with anti-GLUT1 antibodies at 4 °C overnight, followed by incubation with a FITC-conjugated secondary antibody for 2 h. The evaluation of the tumor tissue sections was performed using a Virtual Slide Microscope (VS120−S6−W, Olympus, Japan).

2.10.3. *Mouse tumor models and in vivo antitumor efficacy*

B16−F10 cell suspensions (200 μL, 3×10^6 cells/mL) were injected subcutaneously at the right back of C57BL/6 female mice (CD or HFD). The administration of the therapeutic regimen was commenced once the volume of the B16−F10 tumor had reached 80 mm^3 in 8−10 d after inoculation. The HFD mice were assigned at random into 6 groups ($n = 5$). PBS, aPD-1 (5 mg/kg, intraperitoneally [ip]), Rg3-Lip (4 mg/kg, intravenously [*iv*]), CEL-Lip (2 mg/kg, iv), CR-Lip (2 mg/kg, iv), and CR-Lip + aPD-1 (2 mg/kg CR-Lip, iv + 5 mg/kg aPD-1, ip) were administered. During the treatment period, B16−F10 tumor-bearing HFD mice were maintained on an HFD diet, which is consistent with the literature[7,22]. Measurements of body weight and tumor size were undertaken at two-day intervals. V_t was calculated as shown in Eq. (3):

$$V_t = \left(L \times W^2\right) / 2 \tag{3}$$

L was the longest diameter of B16−F10 tumors; W was the shortest diameter of B16−F10 tumors. Finally, remove the tumor and major organs for further H&E and TUNEL staining. Meanwhile, the survival time for each mouse was monitored and survival curves were recorded.

2.10.4. *Immune status investigation*

Single-cell suspensions obtained from tumors and spleen were stained with antibodies to represent the various types of immune cells. First, an anti-CD16/32 antibody was used to block the Fc to avoid the nonspecific adsorption. $CD8^+$ T cells ($CD3^+$ $CD4^-$ $CD8^+$), IFNγ^+ $CD8^+$ T cells ($CD3^+$ $CD8^+$ IFNγ^+), NK cells ($CD3^-$ $NK1.1^+$), Tregs ($CD3^+$ $CD4^+$ $Foxp3^+$), MDSCs ($CD11b^+$ $Gr1^+$), tumor-associated macrophage (TAMs) including M2 ($CD11b^+$ $F4/80^+$ $CD206^+$) and M1 ($CD11b^+$ $F4/80^+$ $CD86^+$) were collected using FCM analyzed by CytExpert software. Cytokines (IL-1β, IL-6, IL-12, IFNγ, TNFα, and TGF-β) were analyzed by ELISA using a single cell suspension of tumor tissue (10 mg/group).

2.11. *ICD effect evaluation*

2.11.1. *In vitro experiment*

The B16−F10 melanoma cell line (5000 cells/well) was grown in 24-well plates and used after overnight treatment with Adip-CM. To detect the CRT marker on the cellular surface, cells were treated with free CEL, CEL-Lip, or CR-Lip at concentrations of 1.6 μmol/L for 4 h. All groups were then fixed, washed, and incubated with CRT primary antibody (1:2000) for 1 h. For intracellular HMGB1 detection, cells were treated with free CEL, CEL-Lip, or CR-Lip at a concentration of 1.2 μmol/L for a period of 12 h. HMGB1 primary antibody (1:200) was added and incubated with cells for 1.5 h. Next, the cells were incubated with an anti-rabbit secondary antibody (1:200) for 1.5 h. Finally, the cells

were mounted with an anti-fluorescence quenching agent containing DAPI. IF images were captured using the CLSM. CRT-positive cells were examined by FCM. HMGB1 and ATP released in the supernatant were quantified following the instructions of the HMGB1 ELISA Kit and the ATP Detection Kit.

2.11.2. *In vivo experiment*

DC maturation ($CD11c^+$ $CD80^+$ $CD86^+$) was detected by FCM analysis of tumor-infiltrating lymph nodes (TILNs). To observe the *in vivo* ICD effects on CRT and HMGB1, the tumors were collected at the conclusion of the experiments for further analysis using IF techniques. Firstly, the sections were washed and fixed. Then, the tissue sections were stained with either anti-CRT (1:200) or anti-HMGB1 (1:200) at 4 °C overnight, and FITC-conjugated second antibody (1:200) for 1.5 h. At last, the cells were affixed with an anti-fluorescence quenching agent containing DAPI to assess by a slide scanner.

2.12. *Molecular docking study*

In order to obtain the three-dimensional (3D) structures of the PHD3 protein targets, the RCSB Protein Data Bank (PDB) and AlphFold databases were consulted. The two-dimensional (2D) structure of CEL was sourced from the PubChem database and transformed into a 3D structure through the utilization of ChemDraw software. Following this, docking of PHD3 protein to CEL was performed using AutoDock Vina. Graphs of active binding sites were generated using PyMOL software.

2.13. *RT-qPCR and WB assays*

RT-PCR was used to examine the cell and intra-tumor expression of GLUT1 and PHD3. RNA was obtained from tumor cells or flash-frozen tumor tissues using TRIzol. cDNA was synthesized *via* the reverse transcription premix kit. Subsequently, RT-qPCR was conducted with SYBR Green Premix qPCR kit, and the data were analyzed using the ΔΔCt method. GAPDH and β-actin were employed as reference genes for the purposes of data normalization.

To measure the GLUT1 and PHD3 protein expression, the B16−F10 cells were collected and lysed. Samples were prepared by dilution and subsequent heating at 100 °C for 15 min. The separation of proteins was achieved through the utilization of gel electrophoresis, which was subsequently transferred to a polyvinylidene difluoride membrane. Subsequently, the membranes underwent a blocking procedure and were incubated with the primary antibody (4 °C, 12−16 h). The membrane was incubated with the secondary antibody (RT, 1 h) and then chemiluminescence.

2.14. *In-vivo safety evaluation*

Following the completion of the sixth treatment, a sample of whole blood was obtained for the purpose of conducting routine blood analyses. Alanine aminotransferase (ALT) and aspartate aminotransferase (AST) in serum were used to assess hepatotoxicity, and blood urea nitrogen (BUN) and creatinine (CREA) in serum were utilized to assess renal function, creatine kinase-MB (CK-MB) were used to evaluate cardiotoxicity using the serum.

2.15. *Statistical analysis*

Each relevant experiment was performed a minimum of 3 times, and results were expressed as mean ± SD deviation. Analyses of survival rates employed the log-rank test, while other statistical assessments utilized the Student's *t*-test (two-tailed) and one-way ANOVA. Statistical significance was set at $*P < 0.05$.

3. Results and discussion

3.1. *Preparation and characterization of CR-Lip*

CEL-loaded liposomes were synthesized using the thin film dispersion method (Fig. 1A). A Rg3 to SPC ratio of 1:7 was optimized to achieve an appropriate surface charge and size conducive to *in vivo* stability (Fig. 1B). Both CEL-Lip and CR-Lip exhibited mean particle sizes of 126.32 ± 1.17 nm and 116.50 ± 0.72 nm, respectively, with negative zeta potentials (Table 1 and Supporting Information Fig. S1A). The difference in particle size is likely due to the hydrophilic area occupied by Rg3 and Cho. Rg3 has been shown to significantly reduce membrane micropolarity and increase hydrophobicity within the bilayer compared to Cho-Lip, likely due to its strong interaction with phospholipid molecules. Additionally, Rg3 enhances membrane order and liposome stability by immobilizing phosphatidylcholine amine groups *via* hydrogen bonding and restricting acyl chain movement[35]. As a result, CR-Lip outperformed CEL-Lip in several key metrics, including particle size distribution (∼0.12), encapsulation efficiency (∼97%), and drug loading capacity (∼5.7%) (Fig. 1C and D). TEM analysis further confirmed that CR-Lip maintained a uniform spherical morphology (Fig. 1C). Stability studies revealed that CR-Lip remained stable at 4 °C for 7 days (Fig. S1B). Upon incubation at 37 °C for 24 h in PBS containing 10% FBS, CR-Lip exhibited only a minor increase in particle size and PDI (Fig. 1E), indicating robust stability in a simulated blood environment. *In vitro* release studies in PBS at pH 7.4, mimicking the physiological conditions of the blood, demonstrated that CR-Lip provided a more controlled release profile compared to CEL-Lip. CR-Lip achieved approximately 65% cumulative CEL release after 12 h, whereas CEL-Lip released nearly 90% of CEL. Free CEL showed a rapid and complete release within 2 h (Fig. 1F). These findings underscore that CR-Lip offers superior size uniformity, encapsulation efficiency, and stability, as well as a more prolonged release profile compared to CEL-Lip. Such characteristics are likely to enhance the efficacy of CR-Lip in targeting tumor sites more effectively.

3.2. *Improved cellular uptake of Rg3-Lip via Rg3-GLUT1 interaction in Adip-CM-treated tumor cells*

To elucidate the interaction between obesity and melanoma cells, mature adipocytes were differentiated from 3T3-L1 pre-adipocytes to produce Adip-CM. Notable morphological changes were observed, with differentiated adipocytes displaying a significant increase in lipid droplet size and content compared to 3T3-L1 pre-adipocytes (Fig. 2A). Following treatment with Adip-CM, B16−F10 cells exhibited a substantial increase in colony formation, from 55 to 148 colonies (Fig. 2B and C).

The glucose moiety in Rg3 interacts with GLUT1 receptors on the cell membrane[40,41]. Experimental data revealed that the uptake of Rg3-Lip in B16−F10 cells was significantly inhibited by glucose transporter inhibitors such as quercetin[42,43] and was competitively blocked by free glucose. In contrast, no significant difference in uptake efficiency was observed with control liposomes (Cho-Lip) (Fig. 2D and E). This suggests that GLUT1-

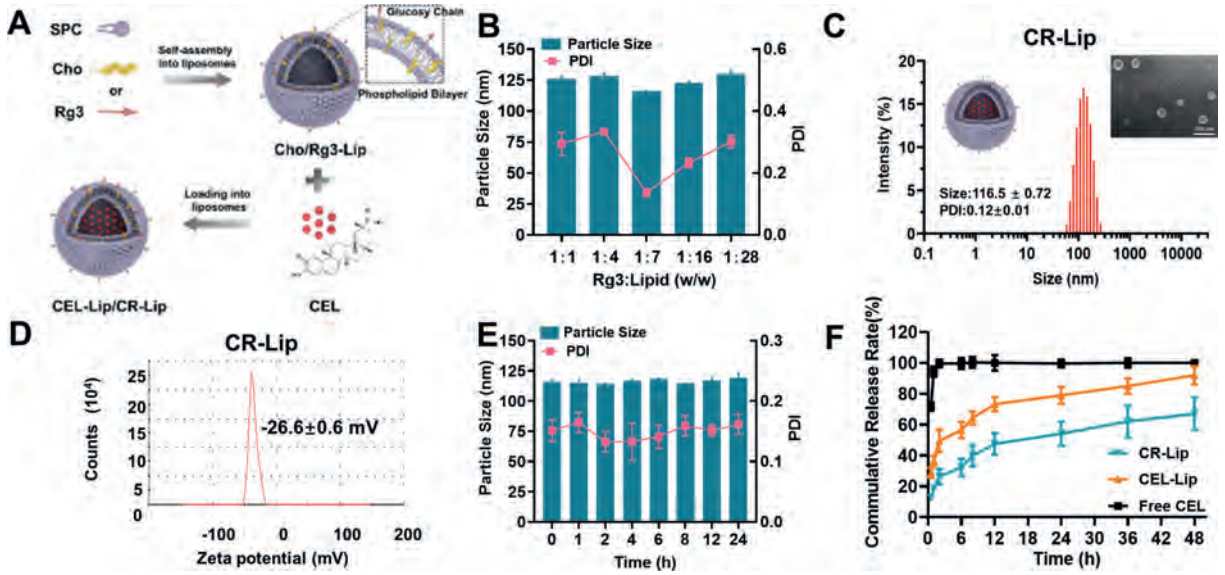

Figure 1 Characterization of CR-Lip and preparation of mature adipocytes. (A) Schematic diagram of constitution (B) Particle sizes and PDI of CR-Lip at different weight ratios of Rg3 to SPC ($n = 3$). Size, TEM images (C) and zeta potential (D) of CR-Lip. (E) Serum stability of CR-Lip by measuring the size change over time ($n = 3$). (F) Cumulative release profiles of CR-Lip at varied conditions ($n = 3$).

Table 1 Particle size, PDI, zeta potential, EE%, and DL% of CEL-loaded Lips.

Vehicle	Particle size (nm)	PDI	Zeta potential (mV)	EE%	DL%
CEL-Lip	126.00 ± 1.17	0.17 ± 0.03	−22.5 ± 0.8	88.23 ± 1.39	5.23 ± 0.08
CR-Lip	116.50 ± 0.72	0.12 ± 0.01	−26.6 ± 0.6	97.58 ± 0.9	5.74 ± 0.05

Data are presented as mean ± SD ($n = 3$). *$P < 0.005$. ns, not significant. PDI, polymer dispersity index; EE%, encapsulation efficiency; DL%, drug-loading; Lip, liposomes.

mediated transport is a crucial mechanism for the cellular uptake of Rg3-Lip by tumor cells. Interestingly, the expression of glycolytic markers (*e.g.*, GLUT1, Pyruvate kinase isozyme type M2, and Lactate dehydrogenase) varied across tumor samples[7]. The effect of obesity on GLUT1 expression on the surface of tumor cells remains unclear. To investigate whether dietary factors influence GLUT1 levels, B16−F10 tumor cells were pretreated with Adip-CM for 24 h. WB and RT-qPCR analyses indicated that Adip-CM treatment led to increased GLUT1 protein and mRNA expression in B16−F10 cells (Fig. 2F−H). Cellular uptake studies using DID-labeled liposomes demonstrated that the median fluorescence intensity (MFI) in B16−F10 cells treated with Rg3-Lip was approximately 1.3-fold higher compared to the Cho-Lip group (Fig. 2I−K). This enhanced uptake is likely due to the elevated expression of GLUT1 on tumor cells. Notably, the uptake efficiency of Rg3-Lip was further augmented by Adip-CM treatment, increasing by approximately 1.6-fold. This observation indirectly supports the hypothesis that Rg3-Lip is transported into tumor cells *via* GLUT1, particularly in HFD tumor cells.

3.3. CR-Lip enhanced cytotoxicity, induced apoptosis and stimulated ICD

The MTT assay was utilized to evaluate the *in vitro* therapeutic efficacy of CR-Lip. Both free Rg3 and Rg3-Lip demonstrated minimal cytotoxicity against B16−F10 cells, indicating the biosafety of the liposome formulation *in vitro* (Supporting Information Fig. S2). In contrast, the free CEL/Rg3 combination therapy induced cytotoxicity in B16−F10 cells, with an IC_{50} of approximately 1.71 μmol/L, and free CEL exhibited a similar IC_{50} (∼1.73 μmol/L). Notably, CR-Lip exhibited superior cytotoxicity compared to other treatments, with an IC_{50} of 1.37 μmol/L (Fig. 2L). To assess the apoptotic efficacy of CR-Lip, apoptosis was evaluated using Annexin V-FITC/PI staining (Fig. 2M and N). The proportion of apoptotic cells (both early and late) was approximately 16.3% for free CEL, 18.5% for CEL-Lip, and 26.9% for CR-Lip. The FCM results indicated that B16−F10 cells treated with CR-Lip showed the highest apoptosis-inducing effect among all groups, even in the absence of Adip-CM. Furthermore, with Adip-CM, the apoptosis rate in B16−F10 cells treated with CR-Lip increased to 40%.

Recent studies have highlighted that ICD can not only induce immunogenic apoptosis in cancer cells but also elicit an anti-tumor immune response[18,44]. We next investigated the ICD-induction potential of CR-Lip. The exposure of CRT on the surface of B16−F10 cells was assessed by FCM. As shown in Fig. 3A and B, CR-Lip significantly increased the CRT^+ cell ratio, which was three times higher than that of the control group. CLSM images revealed that cells treated with CR-Lip exhibited stronger green fluorescence compared to the CEL-Lip group, reflecting increased CRT exposure due to elevated GLUT1 expression on HFD tumor cells (Fig. 3C). ICD is also typically

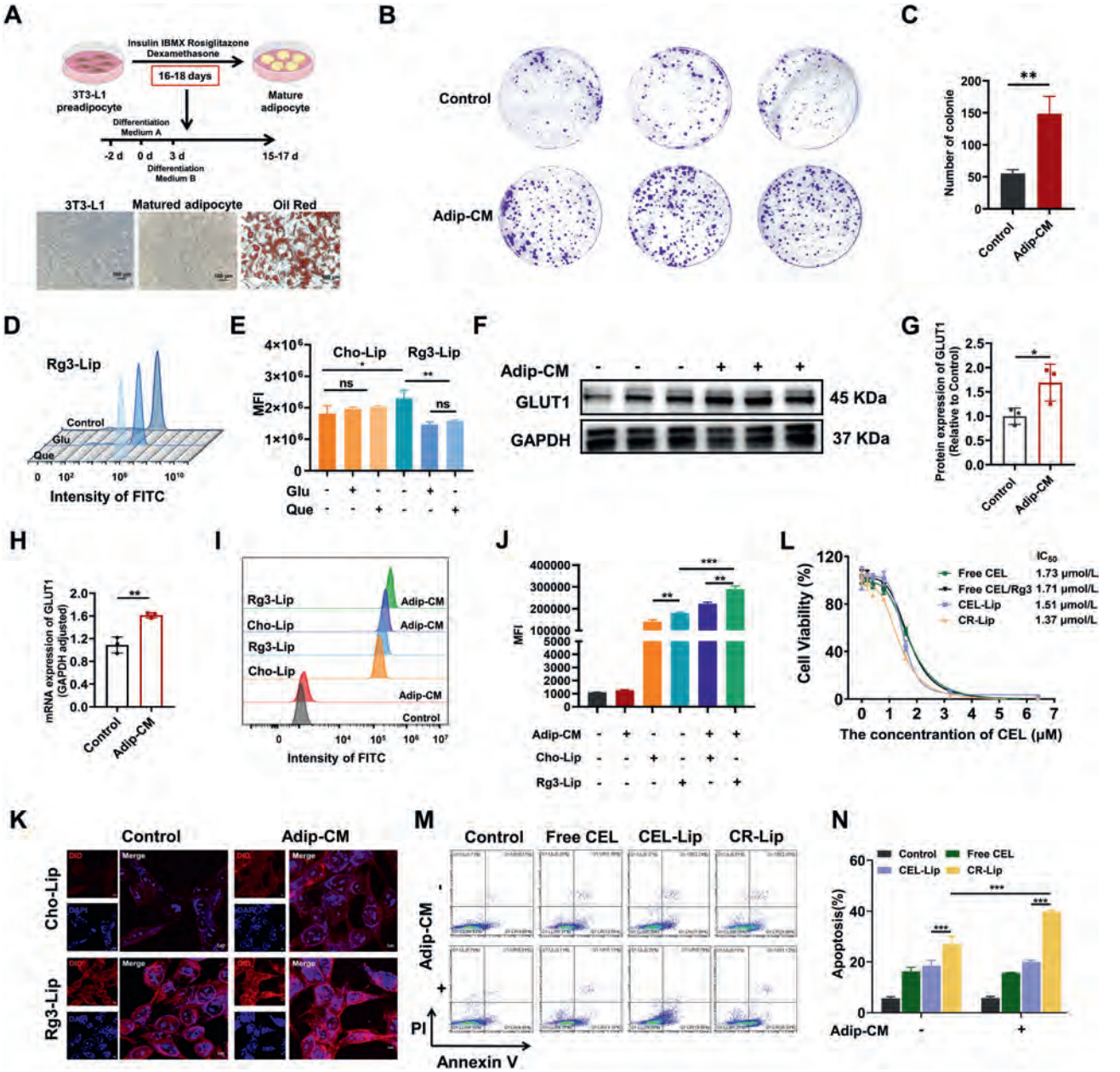

Figure 2 Cellular uptake, cytotoxicity and apoptosis assays *in vitro*. (A) Schematic diagram of the differentiation of mature adipocytes from pre-adipocyte 3T3-L1. (B,C) Colony formation assay of B16−F10 cells cultured with Adip-CM ($n = 3$). (D,E) Cellular uptake of Rg3-Lip with GLUT inhibitor as determined by FCM ($n = 3$). (F,G) GLUT1 expression levels in B16−F10 cell by WB and RT-qPCR (H) after Adip-CM treatment ($n = 3$). Cellular uptake of CEL-Lip and CR-Lip by FCM (I,J) and (K) CLSM analysis. Scale bar = 5 μm. Cell viability (L) and cell apoptosis (M,N) treated with various CEL formulations against Adip-CM treated B16−F10 cells ($n = 3$). $^{*}P < 0.05$, $^{**}P < 0.01$, $^{***}P < 0.001$.

associated with the release of ATP and HMGB1. The levels of ATP secretion and HMGB1 release were measured. CLSM and ELISA assays showed that HMGB1 was released from the nuclei of B16−F10 cells following CR-Lip treatment, with CR-Lip inducing a two-fold increase in HMGB1 release compared to the control (Fig. 3D and E). Additionally, CR-Lip led to the highest ATP release among all treatment groups (Fig. 3F). Overall, these results demonstrate that CR-Lip effectively enhances the "eat me" signal with an ICD mechanism, suggesting its potential role in antitumor immunity.

3.4. CEL regulated lipid availability in HFD tumor cells by enhancing PHD3 expression

Recent studies have reported marked metabolic adaptations in tumors and $CD8^{+}$ T cells in response to obesity[7]. Tumor cells exhibit increased lipid uptake in HFD conditions, whereas tumor-infiltrating $CD8^{+}$ T cells do not. This disparity in metabolic adaptation leads to T-cell impairment as a result of altered FFA partitioning and local exhaustion of critical metabolites, highlighting the interconnected metabolic states of cells in tumors. The

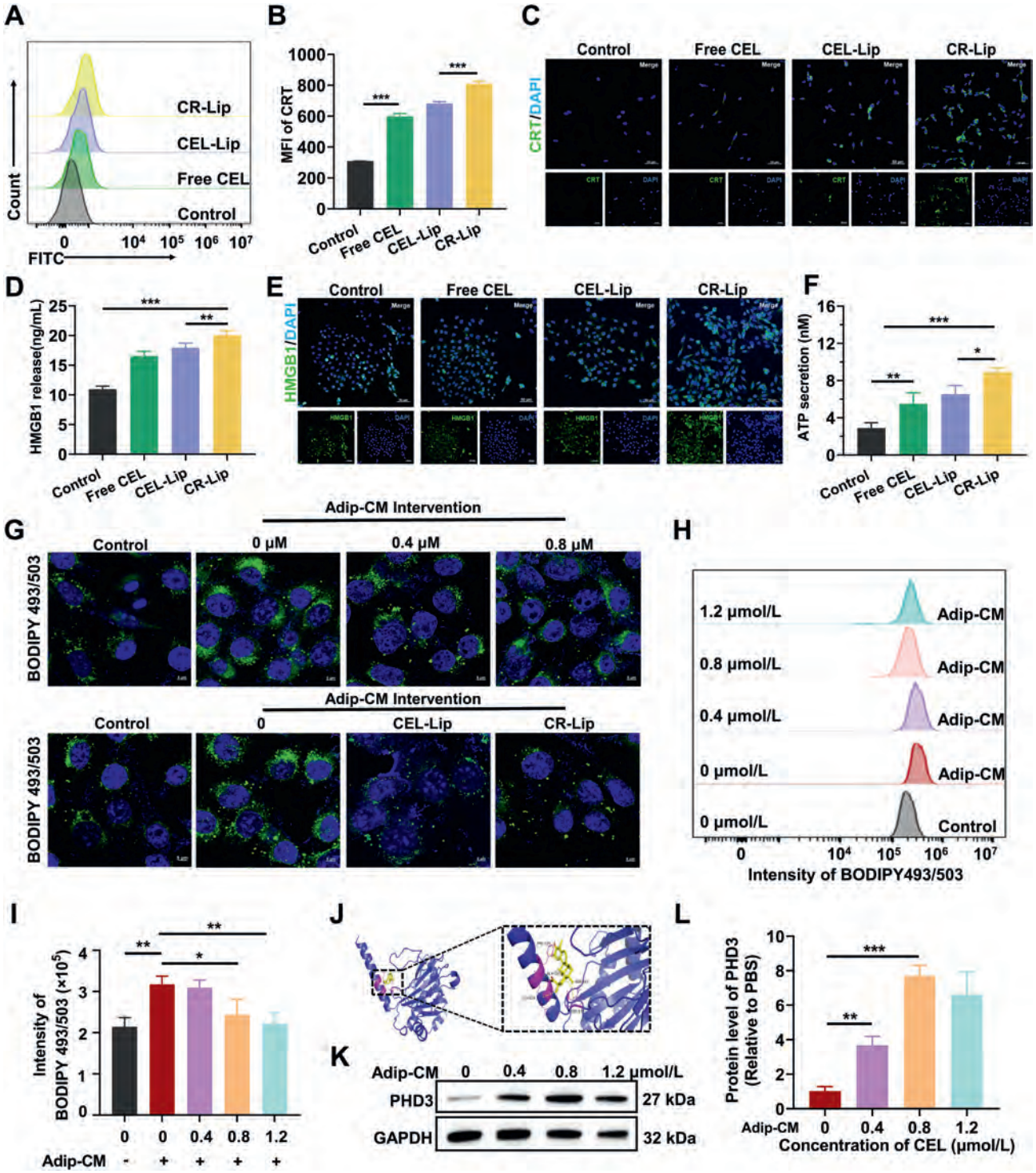

Figure 3 *In vitro* therapeutic mechanisms of CR-Lip. *In vitro* induction of ICD by different CEL formulations: Quantitative FCM analysis (A−B) and the CLSM images (C) of CRT exposure on Adip-CM treated B16−F10 cells ($n = 3$). Scale bar = 50 μm. (D) HMGB1 secretion determined by ELISA kits ($n = 3$). (E) The CLSM images of HMGB1 (Green). Scale bar = 50 μm. (F) ATP secretion from B16−F10 cells treated with varied formulations ($n = 3$). CEL controlled the availability of FFAs: (G) The CLSM images of BODIPY 493/503 (Green) in Adip-CM treated B16−F10 cells after incubating with free CEL (0.4, 0.8, 1.2 μmol/L) and CEL formulations (CEL, 0.8 μmol/L). Scale bar = 5 μm. (H,I) Quantitative FCM analysis of BODIPY 493/503 treated with free CEL ($n = 3$). (J) Molecular docking of CEL complexed with PHD3. (K,L) WB results of PHD3 in Adip-CM treated B16−F10 cells after treatment with CEL ($n = 3$). $^*P < 0.05$, $^{**}P < 0.01$, $^{***}P < 0.001$.

lipid content in B16−F10 cells was assessed using BODIPY 493/503 staining *in vitro*. Prior to the addition of Adip-CM to the culture, B16−F10 cells were incubated with a range of concentrations of CEL, and lipid content was analyzed by CLSM and FCM. As shown in Fig. 3G–I, B16−F10 cells treated with Adip-CM exhibited numerous dense lipid droplets and increased lipid accumulation compared to the control. Interestingly, free CEL effectively reduced lipid levels in a concentration-dependent manner, indicating its capacity to inhibit fat uptake in tumor cells. Furthermore, CR-Lip demonstrated significantly lower tumor lipid accumulation compared to CEL-Lip, likely due to its enhanced liposome uptake efficiency.

Emerging insights into tumor metabolism suggest that obesity downregulates the expression of PHD3 in cancer cells, leading to a depletion of fatty acid fuel sources in the TME. To explore whether the observed changes in fatty acid mobilization in B16−F10 cells after CEL treatment were related to PHD3 regulation, we performed molecular docking of CEL with PHD3 protein structures. The results indicated that CEL has favorable docking potential with PHD3, with a binding affinity of −8.7 kcal/mol, and the active pocket formed by PHD3 was relatively stable (Fig. 3J). Molecular docking revealed that CEL binds to PHD3 through hydrophobic interactions at sites including PHE225, ASN140, ASP142, ALA221, and LYS224. Subsequently, the *in vitro* regulatory effects of free CEL on PHD3 gene expression were evaluated by WB and quantitative analyses (Fig. 3K and L, and Supporting Information Fig. S3). Treatment with CEL (0.4−1.2 μmol/L) significantly upregulated PHD3 expression in a dose-dependent manner. Similarly, the mRNA expression and protein level of PHD3 were markedly increased by CR-Lip (Supporting Information Fig. S4). Collectively, these data support our hypothesis that CEL inhibits the availability of FFAs in tumor cells by modulating PHD3 expression.

3.5. Rg3-Lip enhanced tumor targeting capacity especially in the HFD mouse

To investigate the *in vivo* tumor targeting of CR-Lip following tail vein injection, fluorescence imaging, and biodistribution studies were carried out in B16−F10 tumor-bearing mice. In HFD mice, DiR@Rg3-Lip demonstrated superior tumor retention up to 24 h post-injection compared to DiR@Cho-Lip, which exhibited a significantly weaker fluorescence signal at the tumor site (Fig. 4A).

After 24 h, tumors and major organs were harvested to assess the distribution of various liposome formulations *via* fluorescence intensity (Fig. 4B). As observed with other nanoparticle drug delivery systems[45], both Rg3-Lip and Cho-Lip were predominantly distributed in macrophage-related organs, such as the liver and spleen, with lesser accumulation in other organs (Fig. 4B). Interestingly, we found that Rg3-Lip accumulated more in the liver compared to Cho-Lip, likely due to the smaller particle size and the significantly prolonged circulation time of Rg3-Lip[34] (Table 1). Furthermore, DiR@Rg3-Lip exhibited 2.2-fold higher tumor accumulation than DiR@Cho-Lip (Fig. 4C). As anticipated, in HFD mice bearing B16−F10 tumors, DiR@Rg3-Lip demonstrated 1.3-fold higher tumor accumulation compared to CD mice, attributable to the higher GLUT1 levels, whereas no significant difference was observed with DiR@Cho-Lip.

To further elucidate the distribution of Rg3-Lip in tumor tissue, we performed IF staining with an anti-GLUT1 antibody. GLUT1 was found to co-localize with Rg3-Lip, particularly in tumors of HFD mice (Fig. 4D), indicating that GLUT1-mediated delivery is a crucial mechanism for effective tumor targeting and ablation.

3.6. Evaluation of CR-Lip-mediated combination therapy with aPD-1 in B16−F10 tumor-bearing mice on a HFD

Obesity has been closely linked to the initiation and progression of various cancers, including breast cancer, colorectal cancer, and melanoma[46–48]. To establish a human obesity model in mice, C57BL/6 mice (5-week-old) were randomly assigned to either a CD group or a HFD group, with ad libitum feeding (Fig. 5A). After 8−10 weeks, HFD mice exhibited significant weight gain (∼35.5 g) (Fig. 5B) and developed systemic obesity-associated metabolic abnormalities, including hypercholesterolemia, hypertriglyceridemia, and hyperglycemia (Fig. 5C and Supporting Information Fig. S5). We have also compared the shape and weight of the livers between the CD and HFD groups (Supporting Information Fig. S6). Notably, the livers of HFD mice exhibited a pale or yellow coloration due to fat accumulation, in contrast to the bright red livers of CD mice[49]. This finding aligns with the liver weight analysis. Subsequently, mice were inoculated with B16−F10 melanoma cells. Consistent with prior observations, tumors in HFD-fed mice grew more rapidly compared to those in CD-fed mice[7,22,50,51] (Fig. 5D). Eighteen days post-inoculation, mice were euthanized, and tumors were harvested for further analysis. Tumors from HFD mice showed significantly increased weight compared to those from CD mice (Fig. 5E). H&E and Oil Red O staining of tumors from CD and HFD mice revealed a notable difference in fat content. Tumors from the HFD group contained abundant lipid droplets and increased adipocyte infiltration compared to those from the CD group (Supporting Information Fig. S7). Additionally, FCM analysis of single-cell suspensions from tumors revealed a marked decrease in the percentage of $CD3^+$ $CD8^+$ T cells and $IFN\gamma^+$ within $CD3^+$ $CD8^+$ T cells in HFD mice, indicating impaired T cell infiltration and function (Supporting Information Fig. S8A–S8C). ELISA of cytokine levels in tumor tissues also showed that proinflammatory cytokines (IL-1β, IL-6, IL-12, TNF-α, and IFNγ) were downregulated while anti-inflammatory cytokines (TGF-β) were upregulated in HFD tumors compared to CD tumors (Fig. S8D–S8I). These results suggest that obesity exacerbates the ITME and promotes tumor growth.

To evaluate the anti-tumor efficacy of CR-Lip in combination with aPD-1 therapy, B16−F10 tumor-bearing HFD mice were treated with various formulations once tumors reached approximately 80 mm^3. Treatments included PBS, aPD-1 (5 mg/kg, ip), Rg3-Lip (Rg3, 4 mg/kg, iv), CEL-Lip (CEL, 2 mg/kg, iv), CR-Lip (CEL, 2 mg/kg, iv), and the combination of CR-Lip + aPD-1 (CEL, 2 mg/kg, iv + aPD-1, 5 mg/kg, ip) (Fig. 5F). As illustrated in Fig. 5G–I, PBS, aPD-1, and Rg3-Lip groups exhibited rapid tumor growth, indicating minimal anti-tumor efficacy. In contrast, CEL-Lip, CR-Lip, and CR-Lip + aPD-1 demonstrated varying degrees of tumor regression. Notably, CR-Lip treatment resulted in a significantly higher tumor inhibition rate (∼61.2%) compared to CEL-Lip (∼40.4%) (Fig. 5J), highlighting the enhanced tumor-targeting efficacy of CR-Lip. Remarkably, the combination therapy (CR-Lip + aPD-1) achieved a substantial tumor inhibition rate of 82.1%, outperforming both the aPD-1 group (∼20.8%) and the CR-Lip group (∼61.2%), demonstrating that CR-Lip enhances the sensitivity of B16−F10 tumors to aPD-1. Furthermore, median survival time was significantly prolonged in the combination therapy group (Fig. 5K). Histological analysis *via* H&E and

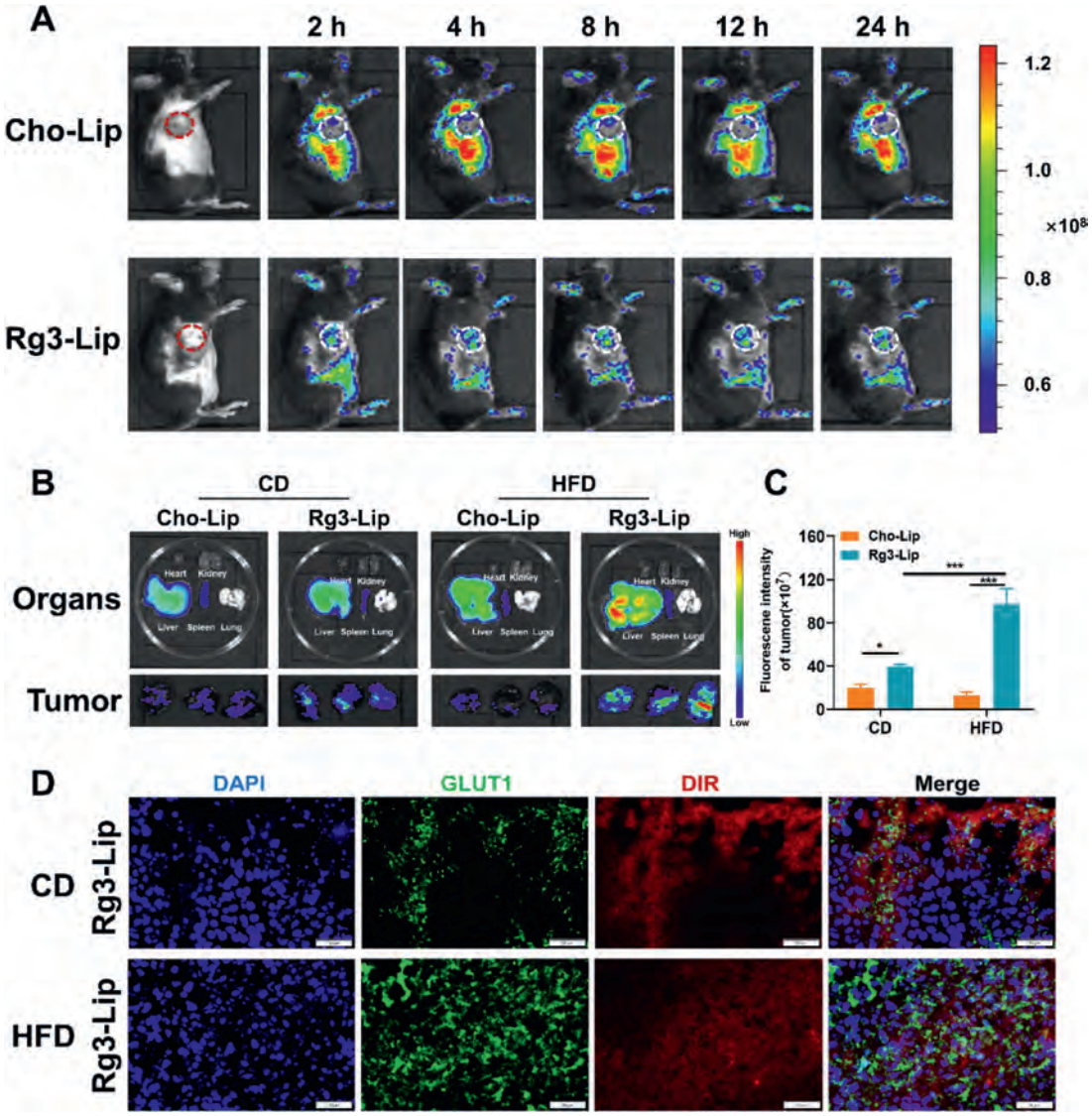

Figure 4 *In vivo* biodistribution. (A) The IVIS images of DiR@Rg3-Lip and DiR@Cho-Lip after administration over time in B16−F10 bearing HFD mice (B) *Ex vivo* monitoring of tumors and major organs after 24 h of *iv* injections. (C) Fluorescence intensity of tumors ($n = 3$). (D) The intratumoral distribution of the DiR@Rg3-Lip and DiR@Cho-Lip (scale bar = 50 μm). $^{*}P < 0.05$, $^{***}P < 0.001$.

TUNEL staining confirmed significant apoptosis in tumors treated with the CR-Lip combined with aPD-1 compared to other groups (Fig. 5L). Overall, these findings underscore the synergistic potential of CR-Lip combined with aPD-1 for improving the treatment of obesity-associated tumors.

3.7. CR-Lip mitigates the ITME to enhance aPD-1 therapy in B16−F10 tumor-bearing HFD mouse model

Given the observed delay in tumor progression with CR-Lip + aPD-1 therapy, we probed the mechanistic basis of this synergistic antitumor effect. We conducted comprehensive FCM analyses to elucidate the impact of CR-Lip + aPD-1 on immune cell populations within tumors from B16−F10-bearing HFD mice. Our analysis focused on DCs maturation, a pivotal marker of immune activation. We assessed the frequency of mature DCs ($CD11c^{+}$ $CD86^{+}$ $CD80^{+}$) in TILNs on Day 15 post-treatment (Fig. 6A and B). Remarkably, CEL treatment alone significantly enhanced DC maturation, reflecting its role in driving ICD *in vivo*. Both CR-Lip and the combination therapy markedly amplified the mature DCs population, approximately 5-fold compared to the PBS control. In contrast, aPD-1 monotherapy failed to elicit significant DCs activation, highlighting a critical limitation of aPD-1 therapy in isolation. The enhanced DCs maturation observed with CR-Lip and CR-Lip + aPD-1 underscores the synergistic effect of Rg3-GLUT1 targeting in augmenting immune activation.

DCs are instrumental in pathogen recognition and the activation of adaptive immunity, particularly T lymphocytes[52,53]. FCM revealed that $CD8^{+}$ T cells constituted 17.72% of the TILNs in the combination therapy group, representing a 2.9-fold increase over the control group (Fig. 6C). Additionally, CR-Lip + aPD-1 significantly boosted IFNγ production by $CD8^{+}$ T cells, surpassing levels observed in other treatment groups (Fig. 6D). The combo therapy also notably activated $CD4^{+}$ T helper cells, signifying a robust T cell-mediated immune response (Fig. 6E). NK cell populations, essential to innate immunity, surged 4- to 5-

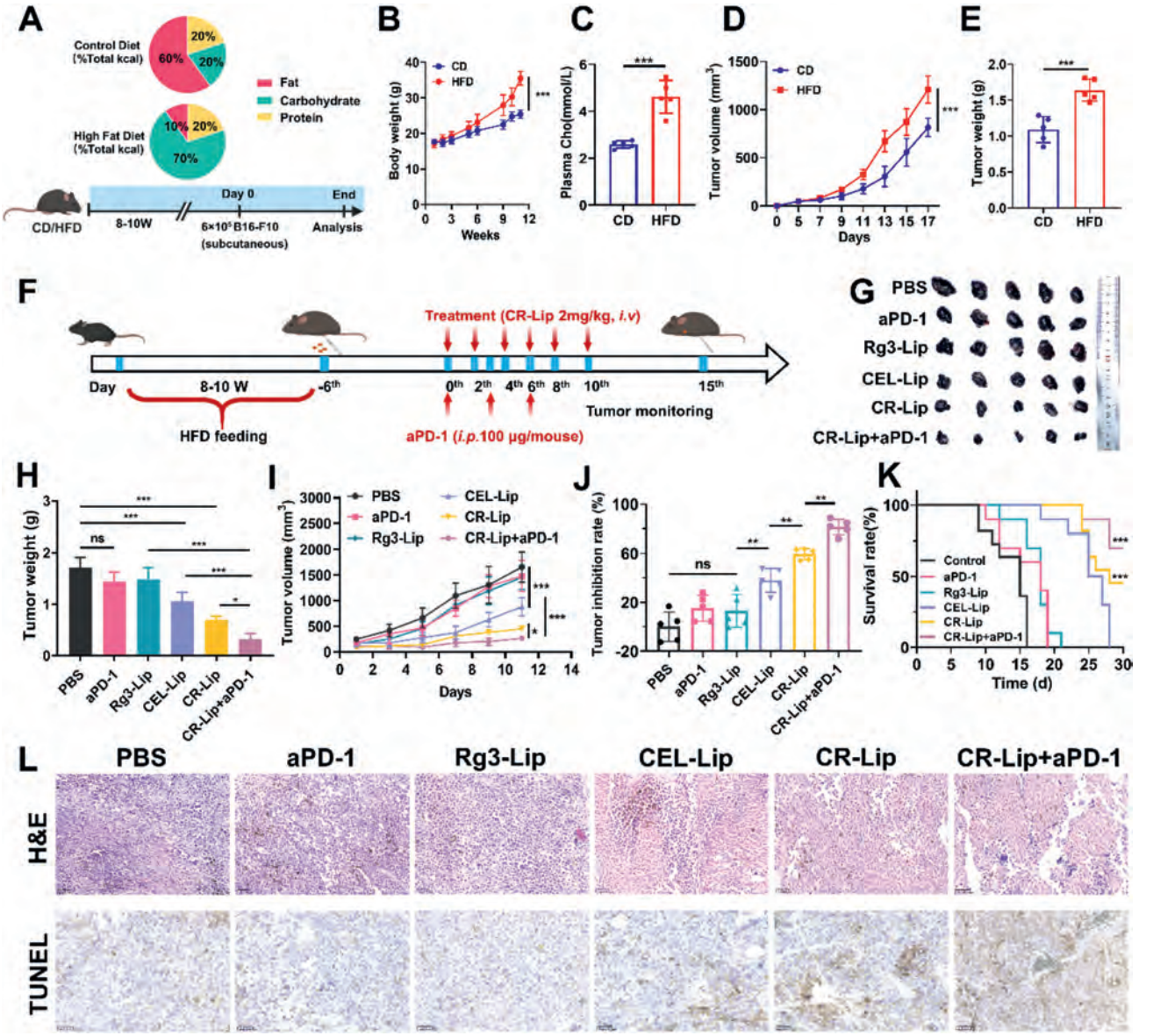

Figure 5 The CR-Lip facilitates the ICB-mediated immunotherapy. (A) Comparing the percentages of kilocalories provided by fat, protein and carbohydrate in the CD and HFD. (B) Body weights ($n = 10$) and (C) the level of plasma Cho ($n = 5$) in C57BL/6 mice after 8−10 weeks of CD or HFD feeding. (D) Tumor volume curve and (E) tumor weight after subcutaneous inoculation of B16−F10 in C57BL/6 mice fed with CD or HFD ($n = 5$). (F) Schematic illustration of performed combination therapy in B16−F10 bearing HFD mice model. (G) Photographs of tumors after treatment ($n = 5$). (H) Weights of tumors and (I) tumor volume changes after treatments ($n = 5$). (J) Tumor inhibition ratio ($n = 5$) and (K) survival curves of mice ($n = 10$). (L) H&E and TUNEL staining images of tumors (scale bar = 50 μm). $^*P < 0.05$, $^{**}P < 0.01$, $^{***}P < 0.001$.

fold in tumors treated with CR-Lip or the combination therapy, whereas aPD-1 alone had no effect (Fig. 6F). Systemic immune responses were further corroborated by analyzing $CD8^+$ T cells in spleens, where the combination therapy induced a substantial increase in both $CD8^+$ T cells and $IFN\gamma^+$ $CD8^+$ T cells (Fig. 6G−J). Moreover, CR-Lip + aPD-1 treatment led to a significant reduction in immunosuppressive cell types, including MDSCs, TAMs, and Tregs, relative to PBS and aPD-1 treatments alone (Fig. 6K and L and Supporting Information Fig. S9). This reduction underscores the ability of CR-Lip + aPD-1 to mitigate the ITME.

Levels of the major pro-inflammatory cytokines IL-6, IL-12, IL-1β, TNF-α, and IFNγ were assessed by ELISA to further characterize the immune response. The combination therapy significantly elevated these cytokines in tumor tissues, indicative of a potent immune activation (Fig. 7C and Supporting Information Fig. S10). Concurrently, TGF-β, an immunosuppressive cytokine associated with tumor progression and immune evasion, was markedly reduced following CR-Lip + aPD-1 treatment. In summary, our findings demonstrate that CR-Lip + aPD-1 treatment profoundly activates DCs and T lymphocytes, effectively counteracting the ITME and enhancing the antitumor response in obesity-associated melanoma. This synergistic approach not only improves immune efficacy but also represents an attractive strategy to tackle the challenges of immunotherapy in obese cancer patients.

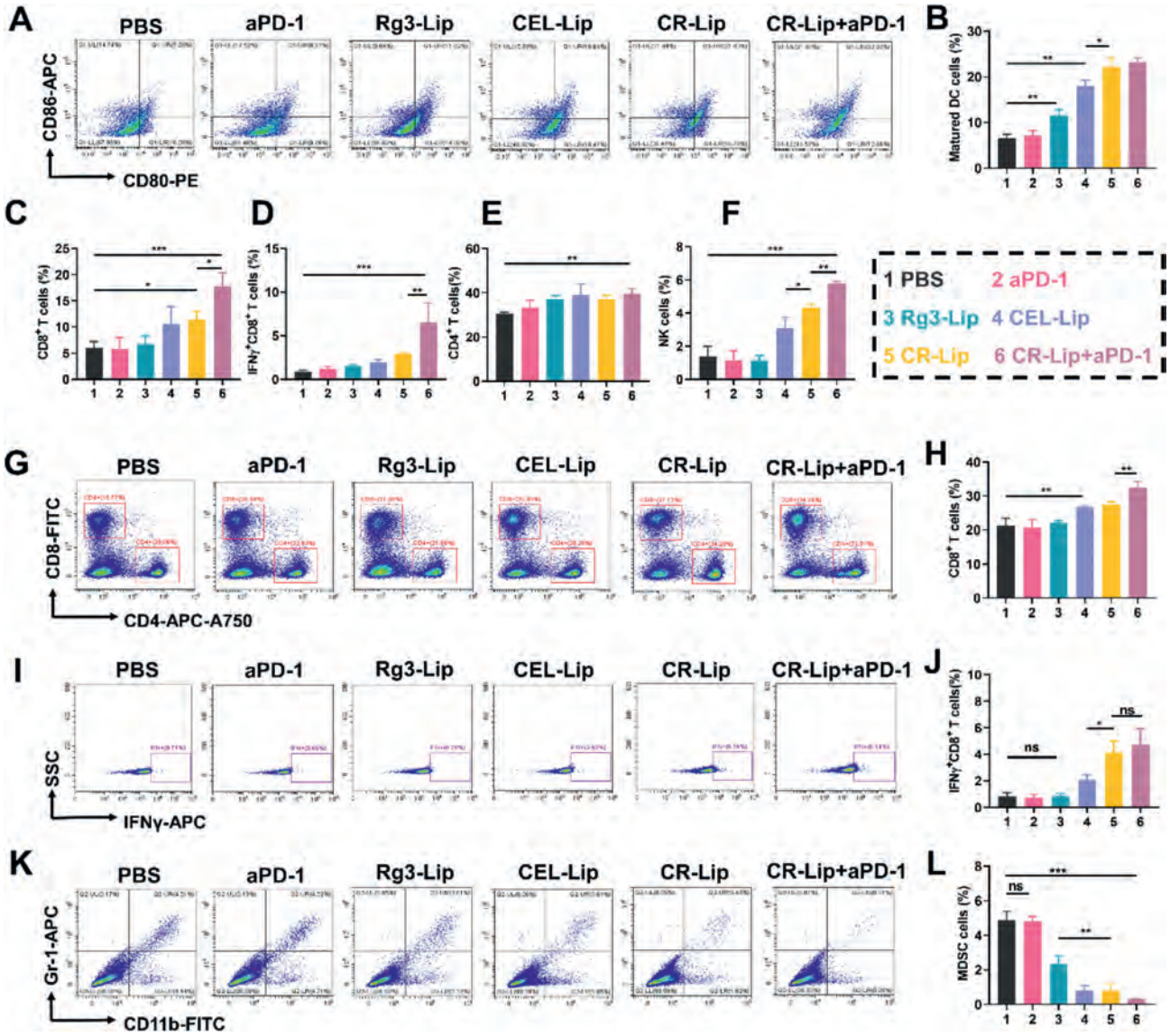

Figure 6 CR-Lip + aPD-1 improves TME in the B16−F10 tumor-bearing HFD mouse. (A,B) FCM results of matured DC in TILNs (gated from $CD11c^+$). Relative abundance of (C) $CD3^+$ $CD8^+$ T cells, and (D) $IFN\gamma^+$ $CD8^+$ T cells in tumor tissues. (E) $CD3^+$ $CD4^+$ T cells, (F) NK cells ($CD3^-$ $NK1.1^+$) in HFD tumors after various treatments. Relative abundance of (G,H) $CD3^+$ $CD8^+$ T cells and (I,J) $IFN\gamma^+$ $CD8^+$ T cells in spleens. (K,L) MDSCs ($Gr\text{-}1^+$ $CD11b^+$) in HFD tumors. $n = 3$, $^*P < 0.05$, $^{**}P < 0.01$, $^{***}P < 0.001$.

3.8. CR-Lip promoted ICD and PHD3 expression in the B16−F10 tumor-bearing HFD mouse

To further elucidate the antitumor mechanisms underlying the CR-Lip + aPD-1 treatment, we performed IF analysis to assess the expression of "eat me" biomarkers, such as CRT and HMGB1. These biomarkers are indicative of ICD and were significantly upregulated in tumor tissues from all CEL-treated groups compared to the PBS control. Notably, CR-Lip treatment resulted in markedly higher staining intensities for CRT and HMGB1 relative to CEL-Lip, suggesting a more pronounced ICD induction (Fig. 7A).

DCs are pivotal in orchestrating a vigorous cytotoxic T lymphocyte (CTL) response. Given the critical role of CTL infiltration in overcoming barriers to effective cancer immunotherapy, we assessed the intratumoral infiltration of $CD8^+$ T cells following CR-Lip + aPD-1 treatment. The results showed a significant elevation in the $CD8^+$ T cell infiltration within tumor tissues in the CR-Lip + aPD-1 group (Fig. 7B). This result underscores the efficacy of CR-Lip in reprogramming the ITME towards an immune-promoting state, thereby facilitating enhanced CTL recruitment and activity in synergy with immune checkpoint blockade (ICB) therapy.

The impact of CR-Lip on the TME was further explored through the evaluation of the expression of PHD3, a key regulator of cellular metabolism and immune responses. In B16−F10 tumors from HFD mice, PHD3 levels were significantly diminished, impairing $CD8^+$ T cell function and infiltration. Our findings, presented in Fig. 7D and E, demonstrate that CR-Lip + aPD-1 treatment markedly upregulates PHD3 expression in tumor tissues. This upregulation likely contributes to the enhanced efficacy of aPD-1 therapy by ameliorating metabolic barriers to immune

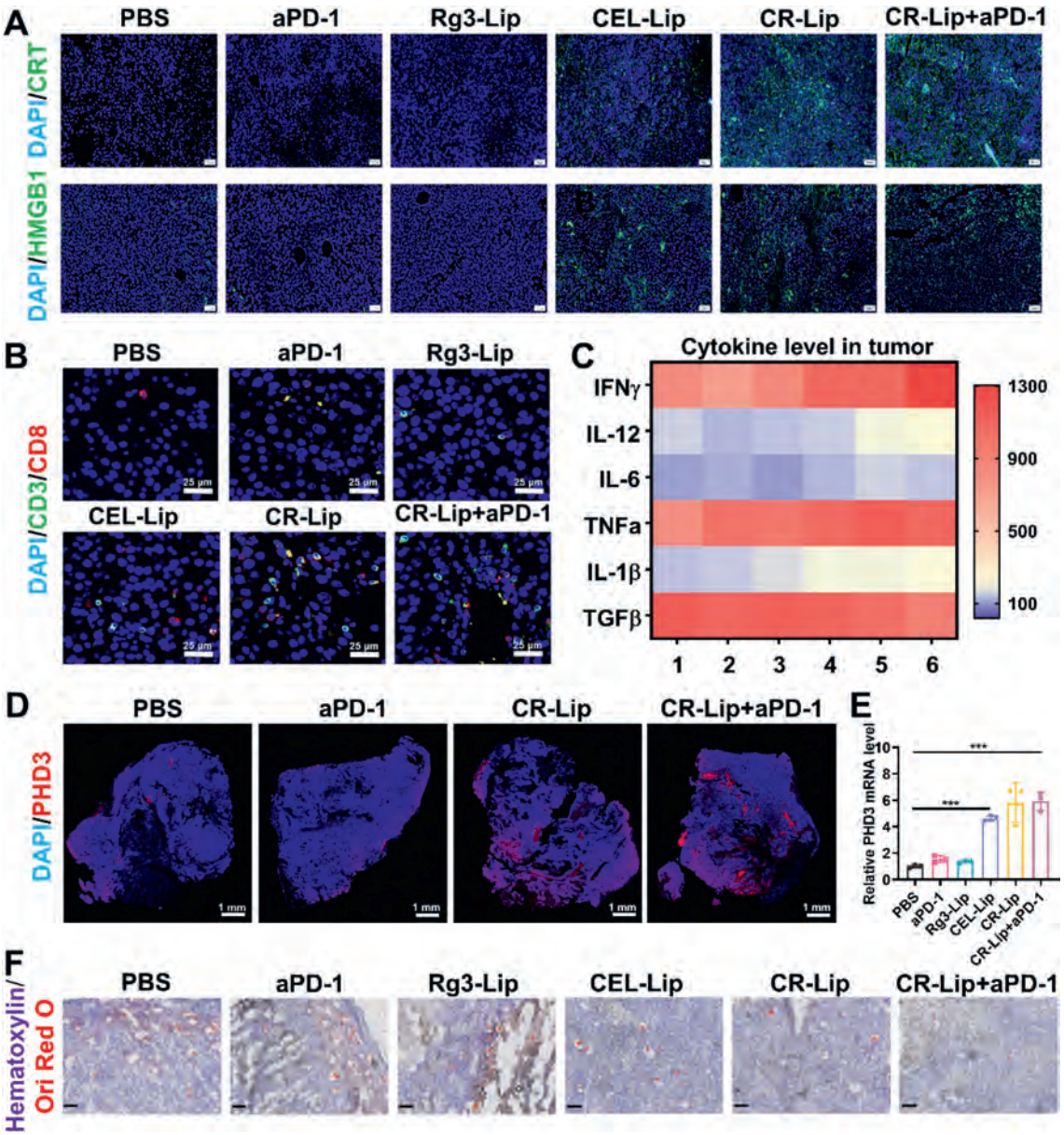

Figure 7 ICD and PHD3 expression in the B16−F10 tumor-bearing HFD mouse. (A) IF images of CRT and HMGB1 in tumors of HFD mice. Scale bar = 50 μm. (B) IF images of CTL infiltration in the tumors. Nucleus: blue color, $CD3^+$ cells: green color, $CD8^+$ cells: red color. Scale bars = 100 μm. (C) Statistical heat map of inflammatory cytokines levels in tumor tissues after treatments ($n = 4$). (D) Representative IF images of PHD3 in the HFD tumors after various treatments. Scale bar = 1 mm. (E) The PHD3 mRNA level in tumors ($n = 3$). (F) Ori Red O staining of the tumor tissues. Scale bar = 100 μm. $***P < 0.001$.

cell infiltration. Additionally, Oil Red O and H&E staining revealed a notable reduction in adipocytes, which are rich in fatty acid droplets, in tumors treated with CEL (Fig. 7F and Supporting Information Fig. S11). This observation suggests that CR-Lip impacts the availability of lipids provided by tumor-associated adipocytes (TAAs)[54−56], potentially alleviating the immunosuppressive TME and impairing the progression of obesity-related melanoma. In summary, our data collectively indicate that CR-Lip + aPD-1 treatment induces significant ICD, enhances CTL infiltration, and upregulates PHD3 in tumors, which collectively remodel the TME to support effective immunotherapy. Furthermore, the reduction in TAAs implies a strategic modulation of lipid availability, which complements the overall therapeutic efficacy of CR-Lip in combating obesity-related melanoma.

3.9. Biosafety evaluation

Despite the known toxicity of CEL[57,58], which limits its clinical application, our study demonstrates that CR-Lip, incorporating CEL, does not exhibit significant adverse effects at a dose of 2 mg/kg. Toxicity assessments revealed no notable variations in hepatic, renal, or cardiac functions (Supporting Information Fig. S12A−S12E), and histological evaluations showed no discernible damage to major organs (Fig. S12F). Surprisingly, all CEL groups (CEL-Lip, CR-Lip, and the combo treatment) efficiently downregulated the body weight loss in the HFD-tumor-bearing mice model (Supporting Information Fig. S13). Emerging evidence highlights CEL's potential in obesity treatment, showing up to 45% weight loss in HFD mice by intraperitoneal for 3 weeks at 100 mg/kg dose and

benefits like improved leptin sensitivity[28], reduced intestinal lipid absorption[59], modulated lipid synthesis and transport[60,61]. These anti-obesity effects likely contribute to the observed weight management in our model, rather than CEL's intrinsic toxicity. Therefore, it can be postulated that the anti-obesity effect of CEL may be the primary factor responsible for the weight loss observed in HFD-tumor-bearing mice model, rather than its intrinsic toxicity. In conclusion, CR-Lip was proven to be safe and potent *in vivo*, with promising prospects for future clinical application.

4. Limitations and outlooks

In view of the obesity impairing the infiltration and function of $CD8^+$ T cells within melanoma in HFD mice, CEL was selected as the therapeutic drug and the developed multifunctional liposomal (CR-Lip) was used to treat the obesity-related tumors by intravenous injection. Notably, CR-Lip not only induced strong ICD in tumor cells but also reprogramed lipid metabolism, likely due to PHD3 upregulation, which significantly improved the immune responsiveness of aPD-1 mediated immunotherapy in B16−F10 melanoma tumor-bearing HFD mice by remodeling obesity-related ITME.

The primary advantage of this liposomal system lies in its simplicity, as it can be manufactured using straightforward components and processes. However, CR-Lip may encounter challenges when transitioning to a clinical setting. These include long-term stability, potential acute toxicity, batch-to-batch variability at the laboratory scale, and complexities in large-scale manufacturing, all of which require further investigation.

As a natural anti-obesity agent, CEL also influences the infiltration of TAAs in tumor tissues, both before and after treatment. TAAs are closely linked to tumor proliferation and the ITME[62]. Therefore, our future studies will focus on the mechanisms by which CR-Lip modulates the interaction between TAAs and tumor cells.

Moreover, dietary stress may exacerbate metabolic conflicts within tumors, directly impacting the functionality of local $CD8^+$ T cells[7,63,64]. Adjusting the dietary regimen of cancer cells has been shown to significantly alter their metabolic activity, leading to changes in drug sensitivity[65], proliferation rates, and metabolic demands[66,67]. Ensuring consistent dietary nutrition throughout the treatment course is thus of critical importance.

Additionally, the metabolic alterations induced by a HFD contribute to tumor growth by suppressing anti-tumor $CD8^+$ T cell responses. Notably, prior studies exploring the link between obesity and cancer have shown that tumor growth kinetics vary across tumor models with different levels of immunogenicity in HFD-fed animals[7], including colorectal adenocarcinoma, breast adenocarcinoma, and Lewis lung cancer. As such, the anti-tumor efficacy of CR-Lip across various HFD-associated tumor models requires further investigation. Moreover, growing evidence suggests that adipose tissue plays a critical role in tumor metastasis[12]. Therefore, CR-Lip's ability to inhibit not only primary tumor growth but also metastasis is essential. Future studies should also examine the long-term effects of CR-Lip on tumor metastasis and its influence on immune memory.

5. Conclusions

We engineered a novel multifunctional liposomal system, CR-Lip, which capitalizes on the unique properties of Rg3 to encapsulate CEL with precision. Our research highlights that GLUT1, a glucose transporter overexpressed in tumor cells under HFD conditions, is a key target for CR-Lip. Rg3 not only enhances membrane integration but also actively targets GLUT1 on HFD tumor cells, facilitating selective and efficient drug delivery. CR-Lip's formulation is both straightforward and effective, enabling it to induce robust ICD. This leads to the activation of DCs, recruitment of cytotoxic $CD8^+$ T cells, and a marked increase in immune cytokine levels, while concurrently reducing immunosuppressive cell populations. Such comprehensive immune activation underscores CR-Lip's potential to reshape the ITME. Importantly, CR-Lip also elevates PHD3 levels in HFD tumor cells, thereby modifying FFA distribution in obesity-driven melanoma. This modulation significantly enhances the therapeutic efficacy of aPD-1 immunotherapy, escalating the tumor inhibition rate from 20.8% with aPD-1 alone to 82.1% with CR-Lip combined with aPD-1. *In vivo* studies validate these findings, demonstrating that CR-Lip, in synergy with aPD-1, not only amplifies systemic anti-tumor immune responses but also prolongs survival in B16−F10 tumor-bearing HFD mice. In conclusion, CR-Lip offers a cutting-edge approach to counteracting the obesity-related ITME. By integrating advanced cytotoxic mechanisms, ICD induction, and targeted metabolic reprogramming, CR-Lip stands at the forefront of innovative strategies to enhance immunotherapy for obesity-associated melanoma, paving the way for future clinical advancements.

Acknowledgments

We appreciate the great help support from the Public Platform of Pharmaceutical Research Center, Academy of Chinese Medical Science, Zhejiang Chinese Medical University. This work was supported by the National Natural Science Foundation of China (82174095), the Natural Science Foundation of Zhejiang Province (LZ22H290001, China), and the Zhejiang Province Traditional Chinese Medicine Science and Technology Project (2023ZL362).

Author contributions

Hongyan Zhang: Writing − original draft, Methodology, Data curation, Conceptualization. Jingyi Huang: Methodology, Formal analysis, Data curation. Yujie Li: Validation, Methodology, Investigation. Wanyu Jin: Methodology, Formal analysis. Jiale Wei: Validation, Software. Ninghui Ma: Validation, Software. Limei Shen: Writing − review & editing. Mancang Gu: Supervision. Chaofeng Mu: Supervision. Donghang Xu: Investigation, Funding acquisition, Conceptualization. Yang Xiong: Supervision, Project administration, Funding acquisition, Conceptualization.

Conflicts of interest

The authors have no conflicts of interest to declare.

Appendix A. Supporting information

Supporting information to this article can be found online at https://doi.org/10.1016/j.apsb.2025.03.017.

References

1. Dyck L, Lynch L. Diverse effects of obesity on antitumor immunity and immunotherapy. *Trends Mol Med* 2023;**29**:112−23.

2. Sung H, Siegel RL, Torre LA, Pearson-Stuttard J, Islami F, Fedewa SA, et al. Global patterns in excess body weight and the associated cancer burden. *CA Cancer J Clin* 2019;**69**:88−112.
3. Lauby-Secretan B, Scoccianti C, Loomis D, Grosse Y, Bianchini F, Straif K, et al. Body fatness and cancer—viewpoint of the IARC working group. *N Engl J Med* 2016;**375**:794−8.
4. Avgerinos KI, Spyrou N, Mantzoros CS, Dalamaga M. Obesity and cancer risk: emerging biological mechanisms and perspectives. *Metabolism* 2019;**92**:121−35.
5. Kyrgiou M, Kalliala I, Markozannes G, Gunter MJ, Paraskevaidis E, Gabra H, et al. Adiposity and cancer at major anatomical sites: umbrella review of the literature. *BMJ* 2017;**356**:j477.
6. Zhang C, Yue C, Herrmann A, Song J, Egelston C, Wang T, et al. STAT3 activation-induced fatty acid oxidation in $CD8^+$ T effector cells is critical for obesity-promoted breast tumor growth. *Cell Metab* 2020;**31**:148-61.e5.
7. Ringel AE, Drijvers JM, Baker GJ, Catozzi A, García-Cañaveras JC, Gassaway BM, et al. Obesity shapes metabolism in the tumor microenvironment to suppress anti-tumor immunity. *Cell* 2020;**183**:1848-66.e26.
8. Weiss SA, Wolchok JD, Sznol M. Immunotherapy of melanoma: facts and hopes. *Clin Cancer Res* 2019;**25**:5191−201.
9. Ribas A, Puzanov I, Dummer R, Schadendorf D, Hamid O, Robert C, et al. Pembrolizumab *versus* investigator-choice chemotherapy for ipilimumab-refractory melanoma (KEYNOTE-002): a randomised, controlled, phase 2 trial. *Lancet Oncol* 2015;**16**:908−18.
10. Kashyap S, Singh MK, Kumar N, Jha J, Lomi N, Meel R, et al. Implications of LAG3 and CTLA4 immune checkpoints beyond PD-1/PD-L1 as a potential target in determining the prognosis of uveal melanoma patients. *Br J Ophthalmol* 2024;**108**:903−12.
11. Chen J, Liu X, Zou Y, Gong J, Ge Z, Lin X, et al. A high-fat diet promotes cancer progression by inducing gut microbiota-mediated leucine production and PMN-MDSC differentiation. *Proc Natl Acad Sci U S A* 2024;**121**:e2306776121.
12. Martin-Perez M, Urdiroz-Urricelqui U, Bigas C, Benitah SA. The role of lipids in cancer progression and metastasis. *Cel Metab* 2022;**34**:1675−99.
13. Bader JE, Wolf MM, Lupica-Tondo GL, Madden MZ, Reinfeld BI, Arner EN, et al. Obesity induces PD-1 on macrophages to suppress anti-tumour immunity. *Nature* 2024;**630**:968−75.
14. Krysko DV, Garg AD, Kaczmarek A, Krysko O, Agostinis P, Vandenabeele P. Immunogenic cell death and DAMPs in cancer therapy. *Nat Rev Cancer* 2012;**12**:860−75.
15. Yamazaki T, Hannani D, Poirier-Colame V, Ladoire S, Locher C, Sistigu A, et al. Defective immunogenic cell death of HMGB1-deficient tumors: compensatory therapy with TLR4 agonists. *Cell Death Differ* 2014;**21**:69−78.
16. Obeid M, Tesniere A, Ghiringhelli F, Fimia GM, Apetoh L, Perfettini JL, et al. Calreticulin exposure dictates the immunogenicity of cancer cell death. *Nat Med* 2007;**13**:54−61.
17. Krysko D. Immunogenic cell death and emission of damps: calreticulin and ATP. *Nanomed Biother Discov* 2012;**2**:860−75.
18. Li Z, Lai X, Fu S, Ren L, Cai H, Zhang H, et al. Immunogenic cell death activates the tumor immune microenvironment to boost the immunotherapy efficiency. *Adv Sci* 2022;**9**:e2201734.
19. Banstola A, Poudel K, Kim JO, Jeong JH, Yook S. Recent progress in stimuli-responsive nanosystems for inducing immunogenic cell death. *J Control Release* 2021;**337**:505−20.
20. Schleh MW, Caslin HL, Garcia JN, Mashayekhi M, Srivastava G, Bradley AB, et al. Metaflammation in obesity and its therapeutic targeting. *Sci Transl Med* 2023;**15**:eadf9382.
21. Hoy AJ, Nagarajan SR, Butler LM. Tumour fatty acid metabolism in the context of therapy resistance and obesity. *Nat Rev Cancer* 2021;**21**:753−66.
22. Fang H, Wu Y, Chen L, Cao Z, Deng Z, Zhao R, et al. Regulating the obesity-related tumor microenvironment to improve cancer immunotherapy. *ACS Nano* 2023;**17**:4748−63.
23. Xue J, Li X, Jiao S, Wei Y, Wu G, Fang J. Prolyl hydroxylase-3 is down-regulated in colorectal cancer cells and inhibits IKKbeta independent of hydroxylase activity. *Gastroenterology* 2010;**138**:606−15.
24. Yano H, Sakai M, Matsukawa T, Yagi T, Naganuma T, Mitsushima M, et al. PHD3 regulates glucose metabolism by suppressing stress-induced signalling and optimising gluconeogenesis and insulin signalling in hepatocytes. *Sci Rep* 2018;**8**:14290.
25. Wang J, Zhang Z, Zhuo Y, Zhang Z, Chen R, Liang L, et al. Endoplasmic reticulum-targeted delivery of celastrol and PD-L1 siRNA for reinforcing immunogenic cell death and potentiating cancer immunotherapy. *Acta Pharm Sin B* 2024;**14**:3643−60.
26. Qiu N, Liu Y, Liu Q, Chen Y, Shen L, Hu M, et al. Celastrol nanoemulsion induces immunogenicity and downregulates PD-L1 to boost abscopal effect in melanoma therapy. *Biomaterials* 2021;**269**:120604.
27. Chen W, Sheng P, Chen Y, Liang Y, Wu S, Jia L, et al. Hypoxia-responsive immunostimulatory nanomedicines synergize with checkpoint blockade immunotherapy for potentiating cancer immunotherapy. *Chem Eng J* 2023;**451**:138781.
28. Liu J, Lee J, Salazar Hernandez MA, Mazitschek R, Ozcan U. Treatment of obesity with celastrol. *Cell* 2015;**161**:999−1011.
29. Feng X, Guan D, Auen T, Choi JW, Salazar Hernández MA, Lee J, et al. IL1R1 is required for celastrol's leptin-sensitization and anti-obesity effects. *Nat Med* 2019;**25**:575−82.
30. He Z, Lieu L, Dong Y, Afrin S, Chau D, Kabahizi A, et al. PERK in POMC neurons connects celastrol with metabolism. *JCI Insight* 2021;**6**:e145306.
31. Xu S, Feng Y, He W, Xu W, Xu W, Yang H, et al. Celastrol in metabolic diseases: progress and application prospects. *Pharmacol Res* 2021;**167**:105572.
32. Greenhill C. Celastrol identified as a leptin sensitizer and potential novel treatment for obesity. *Nat Rev Endocrinol* 2015;**11**:444.
33. Zhu Y, Wang A, Zhang S, Kim J, Xia J, Zhang F, et al. Paclitaxel-loaded ginsenoside Rg3 liposomes for drug-resistant cancer therapy by dual targeting of the tumor microenvironment and cancer cells. *J Adv Res* 2023;**49**:159−73.
34. Xia J, Chen C, Dong M, Zhu Y, Wang A, Li S, et al. Ginsenoside Rg3 endows liposomes with prolonged blood circulation and reduced accelerated blood clearance. *J Control Release* 2023;**364**:23−36.
35. Xia J, Ma S, Zhu X, Chen C, Zhang R, Cao Z, et al. Versatile ginsenoside Rg3 liposomes inhibit tumor metastasis by capturing circulating tumor cells and destroying metastatic niches. *Sci Adv* 2022;**8**:eabj1262.
36. Gyamfi J, Yeo JH, Kwon D, Min BS, Cha YJ, Koo JS, et al. Interaction between CD36 and FABP4 modulates adipocyte-induced fatty acid import and metabolism in breast cancer. *NPJ Breast Cancer* 2021;**7**:129.
37. Ko JH, Um JY, Lee SG, Yang WM, Sethi G, Ahn KS. Conditioned media from adipocytes promote proliferation, migration, and invasion in melanoma and colorectal cancer cells. *J Cel Physiol* 2019;**234**:18249−61.
38. Dai JZ, Wang YJ, Chen CH, Tsai IL, Chao YC, Lin CW. YAP dictates mitochondrial redox homeostasis to facilitate obesity-associated breast cancer progression. *Adv Sci* 2022;**9**:e2103687.
39. Simiczyjew A, Wądzyńska J, Pietraszek-Gremplewicz K, Kot M, Ziętek M, Matkowski R, et al. Melanoma cells induce dedifferentiation and metabolic changes in adipocytes present in the tumor niche. *Cell Mol Biol Lett* 2023;**28**:58.
40. Wang H, Zheng Y, Sun Q, Zhang Z, Zhao M, Peng C, et al. Ginsenosides emerging as both bifunctional drugs and nanocarriers for enhanced antitumor therapies. *J Nanobiotechnology* 2021;**19**:322.
41. Zhang J, Li X, Huang L. Anticancer activities of phytoconstituents and their liposomal targeting strategies against tumor cells and the microenvironment. *Adv Drug Deliv Rev* 2020;**154**−**155**:245−73.
42. Hamilton KE, Rekman JF, Gunnink LK, Busscher BM, Scott JL, Tidball AM, et al. Quercetin inhibits glucose transport by binding to an exofacial site on GLUT1. *Biochimie* 2018;**151**:107−14.

43. Zhu Y, Liang J, Gao C, Wang A, Xia J, Hong C, et al. Multifunctional ginsenoside Rg3-based liposomes for glioma targeting therapy. *J Control Release* 2021;**330**:641−57.
44. Yu S, Xiao H, Ma L, Zhang J, Zhang J. Reinforcing the immunogenic cell death to enhance cancer immunotherapy efficacy. *Biochim Biophys Acta Rev Cancer* 2023;**1878**:188946.
45. Mitchell MJ, Billingsley MM, Haley RM, Wechsler ME, Peppas NA, Langer R. Engineering precision nanoparticles for drug delivery. *Nat Rev Drug Discov* 2021;**20**:101−24.
46. Lagarde CB, Kavalakatt J, Benz MC, Hawes ML, Arbogast CA, Cullen NM, et al. Obesity-associated epigenetic alterations and the obesity-breast cancer axis. *Oncogene* 2024;**43**:763−75.
47. Zheng R, Du M, Zhang B, Xin J, Chu H, Ni M, et al. Body mass index (BMI) trajectories and risk of colorectal cancer in the PLCO cohort. *Br J Cancer* 2018;**119**:130−2.
48. Hahn AW, Menk AV, Rivadeneira DB, Augustin RC, Xu M, Li J, et al. Obesity is associated with altered tumor metabolism in metastatic melanoma. *Clin Cancer Res* 2023;**29**:154−64.
49. Jeong BK, Choi WI, Choi W, Moon J, Lee WH, Choi C, et al. A male mouse model for metabolic dysfunction-associated steatotic liver disease and hepatocellular carcinoma. *Nat Commun* 2024;**15**:6506.
50. Fournier F, Diaz-Marin R, Pilon F, Neault M, Juneau R, Girouard G, et al. Obesity triggers tumoral senescence and renders poorly immunogenic malignancies amenable to senolysis. *Proc Natl Acad Sci U S A* 2023;**120**:e2209973120.
51. Piening A, Ebert E, Gottlieb C, Khojandi N, Kuehm LM, Hoft SG, et al. Obesity-related T cell dysfunction impairs immunosurveillance and increases cancer risk. *Nat Commun* 2024;**15**:2835.
52. Steinman RM. Dendritic cells: versatile controllers of the immune system. *Nat Med* 2007;**13**:1155−9.
53. Pittet MJ, Di Pilato M, Garris C, Mempel TR. Dendritic cells as shepherds of T cell immunity in cancer. *Immunity* 2023;**56**:2218−30.
54. Zhao C, Wu M, Zeng N, Xiong M, Hu W, Lv W, et al. Cancer-associated adipocytes: emerging supporters in breast cancer. *J Exp Clin Cancer Res* 2020;**39**:156.
55. Liu Y, Tiruthani K, Wang M, Zhou X, Qiu N, Xiong Y, et al. Tumor-targeted gene therapy with lipid nanoparticles inhibits tumor-associated adipocytes and remodels the immunosuppressive tumor microenvironment in triple-negative breast cancer. *Nanoscale Horiz* 2021;**6**:319−29.
56. Panaroni C, Fulzele K, Mori T, Siu KT, Onyewadume C, Maebius A, et al. Multiple myeloma cells induce lipolysis in adipocytes and uptake fatty acids through fatty acid transporter proteins. *Blood* 2022;**139**:876−88.
57. Wang S, Liu K, Wang X, He Q, Chen X. Toxic effects of celastrol on embryonic development of zebrafish (Danio rerio). *Drug Chem Toxicol* 2011;**34**:61−5.
58. Zhou M, Liao J, Lai W, Xu R, Liu W, Xie D, et al. A celastrol-based nanodrug with reduced hepatotoxicity for primary and metastatic cancer treatment. *EBioMedicine* 2023;**94**:104724.
59. Hua H, Zhang Y, Zhao F, Chen K, Wu T, Liu Q, et al. Celastrol inhibits intestinal lipid absorption by reprofiling the gut microbiota to attenuate high-fat diet-induced obesity. *iScience* 2021;**24**:102077.
60. Gu J, Shi YN, Zhu N, Li HF, Zhang CJ, Qin L. Celastrol functions as an emerging manager of lipid metabolism: mechanism and therapeutic potential. *Biomed Pharmacother* 2023;**164**:114981.
61. Choi SK, Park S, Jang S, Cho HH, Lee S, You S, et al. Cascade regulation of PPARγ(2) and C/EBPα signaling pathways by celastrol impairs adipocyte differentiation and stimulates lipolysis in 3T3-L1 adipocytes. *Metabolism* 2016;**65**:646−54.
62. Bouche C, Quail DF. Fueling the tumor microenvironment with cancer-associated adipocytes. *Cancer Res* 2023;**83**:1170−2.
63. Zhang Y, Yu X, Bao R, Huang H, Gu C, Lv Q, et al. Dietary fructose-mediated adipocyte metabolism drives antitumor CD8+ T cell responses. *Cel Metab* 2023;**35**:2107−18.e6.
64. Nava Lauson CB, Tiberti S, Corsetto PA, Conte F, Tyagi P, Machwirth M, et al. Linoleic acid potentiates $CD8^+$ T cell metabolic fitness and antitumor immunity. *Cel Metab* 2023;**35**:633−50.e9.
65. Cantor JR, Abu-Remaileh M, Kanarek N, Freinkman E, Gao X, Louissaint A, et al. Physiologic medium rewires cellular metabolism and reveals uric acid as an endogenous inhibitor of UMP synthase. *Cell* 2017;**169**:258−72.e17.
66. Muir A, Danai LV, Gui DY, Waingarten CY, Lewis CA, Vander Heiden MG. Environmental cystine drives glutamine anaplerosis and sensitizes cancer cells to glutaminase inhibition. *Elife* 2017;**6**:e27713.
67. Davidson SM, Papagiannakopoulos T, Olenchock BA, Heyman JE, Keibler MA, Luengo A, et al. Environment impacts the metabolic dependencies of Ras-driven non-small cell Lung cancer. *Cel Metab* 2016;**23**:517−28.